Prediction of Thermodynamic Properties of Sacred Pepper (Piper auritum) Using Machine Learning

Cesar Cesar Pérez-Alonso
Universidad Autónoma del Estado de México
José Alvarez-Ramirez
Universidad Autónoma Metropolitana
Reyna Natividad
Universidad Autónoma del Estado de México
Ever Peralta-Reyes
Universidad del Mar, Campus Puerto Ángel
Alejandro Regalado-Méndez
alejandro_regalado@aulavirtual.umar.mx

Universidad del Mar, Campus Puerto Ángel

Research Article

Keywords: Artificial neural network, Sacred pepper, Machine learning, Random forest, Support vector machine, Thermodynamic properties

Posted Date: January 9th, 2026

DOI: https://doi.org/10.21203/rs.3.rs-8546355/v1

Additional Declarations: No competing interests reported.

Prediction of Thermodynamic Properties of Sacred Pepper (*Piper auritum*) Using Machine Learning

Cesar Pérez-Alonso [1], José Alvarez-Ramirez [2], Reyna Natividad [3], Ever Peralta-Reyes [4], and Alejandro Regalado-Méndez [4, *]

[1] Departamento de Ingeniería Química, Facultad de Química, Universidad Autónoma del Estado de México, Paseo Colón esq. Paseo Tollocan s/n, Col. Residencial Colón, C.P. 50120, Toluca, Estado de México, México.

[2] Departamento de Ingeniería de Procesos e Hidráulica, Universidad Autónoma Metropolitana-Iztapalapa, Apartado Postal 55-535, Iztapalapa, CDMX 09340, Mexico

[3] Chem. Eng. Lab., Joint Centre for Research on Sustainable Chemistry UAEM-UNAM, Faculty of Chemistry, Universidad Autónoma del Estado de México, Toluca 50200, Mexico

[4] Research Laboratories, Universidad del Mar, Campus Puerto Ángel, Puerto Ángel, Oaxaca 70902, Mexico

[*] **Corresponding author:** alejandro_regalado@aulavirtual.umar.mx (A.R.-M.)

https://orcid.org/0000-0002-5270-745X

Abstract

This study compares the application of three Machine Learning (ML) models—Artificial Neural Networks (ANNs), Random Forest (RF), and Support Vector Machines (SVM)—for predicting thermodynamic properties (enthalpy change, ΔH; entropy change, ΔS; and Gibbs free energy change, ΔG) of *Piper auritum*. The models were developed using experimental data correlating these properties with moisture content and temperature. Each model's architecture was optimized: ANNs with a three-layer feedforward structure trained with the Levenberg-Marquardt algorithm, RF with property-specific tree counts, and SVM with a Radial Basis Function kernel. Model performance was evaluated using k-fold cross-validation and metrics including R^2, MAE, MSE, and RMSE. Results show that all three ML approaches effectively capture nonlinear relationships, but ANNs outperformed the others, achieving high R^2 values (e.g., overall $R^2 > 0.999$ for ΔH and ΔS). SVM provided intermediate performance, while RF was the least accurate. ANNs are the most powerful and reliable tool for this regression task, offering a highly accurate computational method to predict thermodynamic behavior and potentially reduce experimental characterization needs.

Keyword: Artificial neural network, Sacred pepper; Machine learning; Random forest; Support vector machine; Thermodynamic properties

Introduction

The use of medicinal plants dates back millennia (Davis and Choisy 2024). Mesoamerica, the region from central Mexico to northern Central America, was home to civilizations such as the Olmecs, Maya, and Aztecs, which extensively used native plants for medicine, rituals, and as cultural symbols (Geck et al. 2020). The legacy of traditional plant medicine remains relevant today, with an estimated 80% of the global population using herbal medicines (Ekor 2014).

Piper auritum, commonly known as "hoja santa" (aka, "sacred pepper") in Mesoamerica and as "root beer plant" in England and USA, is a small, perennial shrub native to Mexico and Central America (Conde-

Hernández and Guerrero-Beltrán 2014). Its large, ear-shaped leaves can reach up to 30 cm in length and emit a distinctive aroma reminiscent of sassafras, anise, and pepper, earning it the name "root beer plant." This plant is valued for its diverse medicinal and culinary applications (McBurnett et al. 2007). In traditional medicine, *P. auritum* is widely used, especially for respiratory ailments. A common preparation is an infusion of tea for bronchitis and throat irritations. The plant is also used to stimulate digestion, relieve colic, and act as a diuretic; crushed leaves are applied topically for skin infections, such as erysipelas. Scientific studies indicate that plant extracts possess antimicrobial properties (Conde-Hernández et al. 2017), supporting some of these uses.

Culinarily, *P. auritum* has a long history dating back to the Aztecs, who used it in the preparation of ceremonial chocolate. It remains a popular ingredient throughout Central America and in regions like Veracruz, Mexico. The leaf is considered essential in dishes such as *mole verde*, one of the traditional "seven sauces of Oaxaca," and is frequently used as an aromatic wrapper for grilling or steaming fillings, most commonly chicken or fish (Bayless and Bayless 2024; Davidow 1999; Sánchez et al. 1986; Williams et al. 2004).

The growing global reliance on medicinal herbs for self-medication heightens the need to ensure their quality and efficacy. A key determinant of postharvest quality is moisture content, which is governed by water vapor adsorption properties. Understanding these properties in herbs like *Piper auritum* is therefore essential for optimizing drying and storage protocols to preserve bioactive compounds (Chong et al. 2023). Adsorption isotherms are a fundamental tool for this purpose, providing critical insight into the thermodynamic interaction between water vapor and the solid matrix of processed plant material, such as crushed leaves.

Sorption isotherms modeled using either empirical (e.g., Oswin, Smith, Henderson, Halsey, Kuhn, among others) or theoretical (e.g., Guggenheim–Anderson–de Boer, GAB, Brunauer–Emmett–Teller, BET) equations (Bensebia and Allia 2016), can be used to estimate thermodynamic properties such as enthalpy (ΔH), entropy (ΔS), and Gibbs free energy (ΔG) of biological materials like dried herbs and their extracts. These thermodynamic properties are crucial for establishing conditions that maximize food stability, which in turn informs the design of key unit operations such as dissolution, crystallization, and drying (Alpizar-Reyes et al. 2017). However, these models are based on specific mechanistic assumptions.

Artificial intelligence (AI) and Machine Learning (ML) pose a key advantage over models based on specific mechanistic assumptions: their ability to learn directly from data without requiring a predefined, theoretically correct equation. This enables ML to model phenomenally complex, high-dimensional, or poorly understood systems, such as image recognition or natural language, where deriving precise mechanistic equations is impossible. While this often yields superior predictive accuracy from large datasets, it comes at the cost of interpretability and reliable extrapolation, areas where traditional mechanistic models, grounded in domain knowledge and causal principles, remain stronger. Consequently, ML excels as a powerful, adaptable pattern-finder for opaque problems, such as the nonlinear processes inherent in food processing, since it allows the identification of complex relationships directly from data (Ben Khedher and Yun 2024; Birgen et al. 2021; Rashvand et al. 2025).

Artificial Neural Network (ANNs) based on a multilayer perceptron (MLP) architecture. The feed-forward network was trained using the back-propagation algorithm, specifically gradient descent with momentum (traingdm), to optimize the connection weights and minimize the prediction error. The structure of the MLP, with its input, hidden, and output layers, is designed such that the number of neurons in the input and output layers corresponds to the independent (e.g., ΔH, ΔS, and ΔG) and dependent variables (e.g., of temperature (T) and moisture (M)), respectively (Razzaghi et al. 2018). Random Forest (RF) and Support Vector Machine (SVM) models are among the most robust models, which help avoid potential overfitting. The RF is an ensemble ML method based on decision trees that uses voting for categorization and averaging for regression (Ullah et al. 2023). Finally, the idea of the support vector machine (SVM) is to map the input vectors x into a high-dimensional feature space Z and memory efficient through some nonlinear mapping, chosen *a priori* (kernel trick, e.g., linear, polynomial, and Radial Basis Function (RBF)) (Vapnik 2000).

ML algorithms have been employed to model moisture sorption isotherms of coffee beans (Collazos-Escobar et al. 2025), non-thermal food processing (Rashvand et al. 2025), roasting degree prediction model of coffee beans (Okamura et al. 2021), drying kinetics of mint branches (de Holanda Rosanova et al. 2017), sorption isotherms of coffee cherry (Velásquez et al. 2021), predicting physicochemical properties of dried onion (Liu et al. 2025), Kiwifruit drying pretreatment (Yu et al. 2024), modeling and optimization of microwave vacuum drying for *Pinelliae Rhizoma* (Wang et al. 2025), optimization of microwave-assisted extraction of phenolic compounds from *Pithecellobium* dulce Fruit Peels (Loganathan et al. 2025), and sorption isotherm in microwave pre-heated mung bean (Kaur et al. 2024). However, existing ANNs models for thermodynamic properties in the literature are limited to enthalpy (ΔH) as a function of moisture content (Barati et al. 2015; Chayjan and Esna-Ashari 2011). This study is the first one modelling the full set of thermodynamic potentials, ΔH, ΔS, and ΔG, as functions of both temperature and moisture content.

The objective of this work was to model and interpret the thermodynamic properties (ΔH, ΔS, and ΔG) of crushed sacred pepper as functions of temperature (T) and moisture content (M), through methods like Machine Learning, Artificial Neural Networks (ANNs), Random Forest (RF), and Support Vector Machines (SVM). These methods were selected for their ability to handle complex, non-linear relationships. The ANNs, RF, and SVM models were developed in the MALAB® 2017a software package.

Methodology

Data Collection

This study utilized an experimental dataset containing the independent parameters—temperature (T) and concentration (M)—and the dependent thermodynamic properties (ΔH, ΔS, and ΔG), as detailed in Table S1 of the supporting material.

Sorption isotherms of crushed sacred pepper

The adsorption isotherms of crushed sacred pepper were obtained by a static gravimetric method for temperatures 25, 35 and 40 °C throughout a water activity (a_w) range from 0.11 to 0.85 (Alpizar-Reyes et al. 2017). The runs were carried out by triplicate. Subsequently, the sorption isotherms were described by the GAB model,

$$M = \frac{M_0 \times C \times K a_w}{\left(1 - K \times a_w\right)\left(1 - K \times a_w + C \times K \times a_w\right)} \tag{1}$$

where T is temperature, M is the monolayer moisture content, K is the difference in the sorbate's pure liquid state and the upper layers, C is the difference in magnitude between higher layers and the monolayer moisture content, and a_w is the water activity.

Thermodynamic Properties Determination

The energetic sorption process characterized by ΔH, ΔS, and ΔG, can be estimated by the set of Eqs. (2)-(4) (Arslan-Tontul 2020; Pérez-Alonso et al. 2006; Rizvi 2014),

$$\left(\frac{\partial Ln\left(a_w\right)}{\partial\left(\frac{1}{T}\right)}\right)=-\frac{\Delta H}{R} \tag{2}$$

$$\Delta S=-\frac{\Delta H}{T}-RLn\left(a_w\right) \tag{3}$$

$$\Delta G=RTLn\left(a_w\right) \tag{4}$$

Artificial Neural Networks (ANNs)

An ANNs was developed to model the relationships between moisture content (*M*) and temperature (*T*) on three thermodynamic properties: the change in Enthalpy (ΔH), Entropy (ΔS), and Gibbs free energy (ΔG). The simulation was conducted using the MATLAB software package (version R2017a, license number 1082300, purchased from Multion Consulting, S.A. de C.V., Mexico). A three-layer feedforward backpropagation network was implemented, utilizing linear (purelin), hyperbolic tangent sigmoid (tansig), and linear (purelin) transfer functions for the input, hidden, and output layers, respectively. The network was trained using the Levenberg–Marquardt algorithm.

The input layer consisted of two numeric parameters (moisture and temperature). Also, the inputs were normalized according to Eq. (5). The output layer includes one neuron for each thermodynamic property: Enthalpy (ΔH), Entropy (ΔS), and Gibbs free energy (ΔG). A total of 105 data points were randomly divided into three categories: training (70%, which consists of 73 points), testing (15%, which consists of 16 points), and validation (15%, which 16 points). This division was established to develop the ANNs model for three response variables: ΔH, ΔS, and ΔG.

All numerical data were normalized to a [0,1] scale using Eq. (5) prior to model development to ensure comparability and improve algorithmic performance. Separately, the relevant kinetic parameters obtained for the GAB model are summarized in Table S2.

$$\xi_k=\frac{x_k-x_{k,\min}}{x_{k,\max}-x_{k,\min}} \qquad k=\Delta H,\ \Delta S,\ and\ \Delta G \tag{5}$$

where x_k are parameters (*M* (Kg H_2O/100 Kg dry solid) and *T* (K)) and ξ are normalized parameters.

The accuracy of the ANNs models in representing the three thermodynamic properties was highly dependent on the network topology. To optimize the architecture, specifically the number of hidden layers and neurons, a trial-and-error approach was used. The generalizability and robustness of the optimal models were subsequently evaluated using k-fold cross-validation.

Figure 1 shows the topology of the ANNs, which is designed so that each neuron in each layer is connected to all neurons in the following layer. These connections have associated weights that indicate the strength of each connection. During the training process, these weights are adjusted and optimized. A neuron in a specific layer calculates the weighted sum of incoming signals and transmits this value to a neuron in the next layer using a transfer function. The relationship between the input parameters (*M* and *T*) and the output layer (responses ΔH, ΔS, and ΔG) can be represented by Eq. (6),

$$Y_i = f_2\left(\sum w_2\left[f_1\left(\sum X_i w_1 + b_1\right) + b_2\right]\right) \quad (6)$$

where X is the input vector, formed by the variables M and T, w_1 is the weight matrix that connects the input layer to the hidden layer, governing the strength of these connections, b_1 is the bias vector for the hidden layer, allowing the activation function to be shifted, f_1 is the activation function applied element-wise to the weighted sum of the inputs and bias at the hidden layer, introducing non-linearity, w_2 is the weight matrix that connects the hidden layer to the output layer, transforming the activated features into the final output, b_2 *is th*e bias vector for the output layer, providing an adjustable offset to the final output calculation, f_2 is the activation function applied to the output layer, which shapes the final network output Y_i appropriately for the task (e.g., linear for regression, SoftMax for classification), Y_i is the final output value or vector produced by the network after the second activation function f_2 is applied.

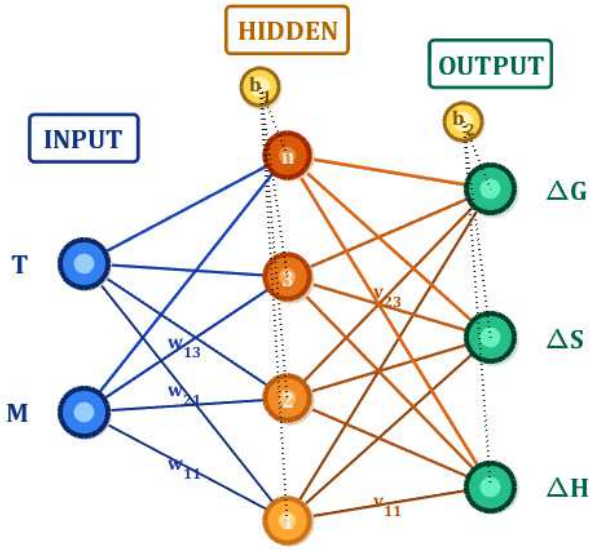

Fig. 1. Topology of the Artificial Neural Networks (ANNs) applied to predict thermodynamic properties, ΔH, ΔS, and ΔG, of sacred pepper leaf.

Random Forest (RF)

The Random Forest (RF) algorithm was employed to construct individual predictive models for the three key thermodynamic properties: ΔH, ΔS, and ΔG. The implemented architecture comprised three distinct forests, each optimized for a specific property (e.g., 50 trees for ΔH, 100 for ΔS, and 20 for ΔG). Model training followed the standard RF approach of bootstrap aggregating, in which each decision tree is generated from a randomly sampled subset of the data and considers a random subset of features at each node. To reduce the risk of overfitting, a minimum leaf size of five samples was specified. Model performance and robustness were evaluated using k-fold cross-validation. Variable importance was determined by calculating the Out-of-Bag (OOB) permutation error. Figure 2 presents a schematic representation of RF architecture.

The relationship between the input layer (parameters M and T) and the output layer (responses ΔH, ΔS, and ΔG) is defined by Eq.(7),

$$\hat{y}(M,T) = \frac{1}{N_{trees}} \sum_{i=1}^{N_{trees}} \psi(M,T)_i \tag{7}$$

where N_{trees} are the number of trees for each thermodynamic property, ψ_i (M, T) is the prediction of i-th tree, and ŷ is the predicted value for each thermodynamic property.

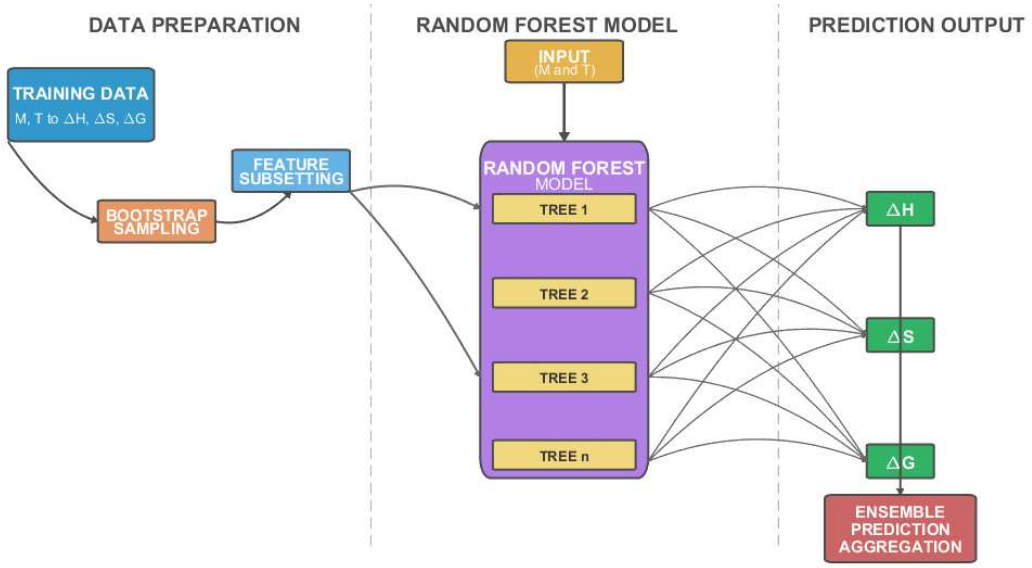

Fig. 2. Random Forest (RF) architecture to predict thermodynamic properties, ΔH, ΔS, and ΔG, of sacred pepper leaf.

Support Vector Machine (SVM)

The predictive framework employs three separate SVM regression models, each utilizing a Radial Basis Function (RBF) kernel, to estimate the thermodynamic properties (ΔH, ΔS, and ΔG). This kernel is chosen for its ability to capture the nonlinear relationships between the input variables (M and T) and the target properties. The models are trained using the Sequential Minimal Optimization (SMO) algorithm, with key hyperparameters (kernel scale, box constraint, and epsilon) optimized automatically via MATLAB's fitrsvm function. The input data was normalized using the mapminmax function prior to training. Predictive performance for all three properties was rigorously validated through k-fold cross-validation and by using separate training, validation, and test datasets. The overall SVM architecture is illustrated in Figure 3.

The relationship between the input layer (parameters M and T) and the output layer (responses ΔH, ΔS, and ΔG) is defined by Eq. (8),

$$f(x) = \sum_{i=1}^{n} \left[\alpha_i - \alpha_i^* \right] K(x_i, x) + b \tag{8}$$

where α_i, α_i^* are the Lagrange multipliers (support vectors), K (x_i, x) is the RBF kernel function, x corresponds to input parameters (M and T), and n is the number of support vectors.

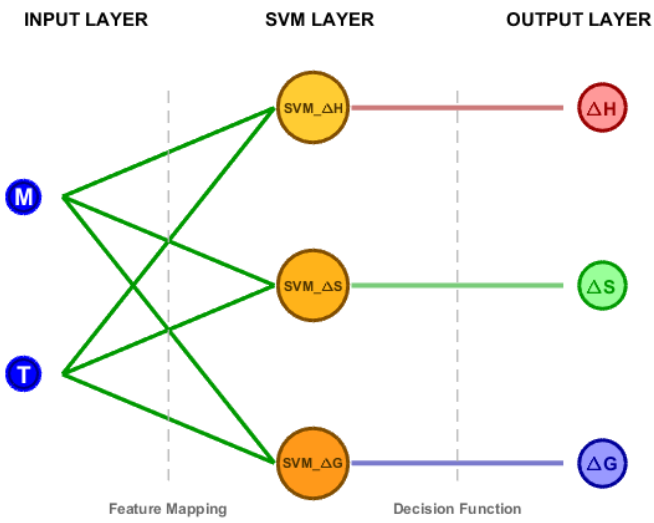

Fig. 3. Overall Support Vector Machine (SVM) model architecture to predict thermodynamic properties, ΔH, ΔS, and ΔG, of sacred pepper leaf.

Accuracy for the Three Different Machine Learning Models

The accuracy of the ANNs, RF, and SVM models for each thermodynamic property was determined using the determination coefficient (R^2), mean square error (MSE), root mean square error (RMSE), and mean absolute error (MAE), and, according to Eqs. (9), (10), (11), and (12), respectively for training, validation, testing, and overall (Mason et al. 2023; Rajawat et al. 2022).

$$R^2 = \frac{\sum_j^n \left(y_{i,\,\exp} - y_{i,\,pred}\right)^2}{\sum_j^n \left(y_{i,\,\exp\_average} - y_{i,\,pred}\right)^2} \tag{9}$$

$$MSE = \frac{\sum_j^n \left(y_{i,\,\exp} - y_{i,\,pred}\right)^2}{n} \tag{10}$$

$$RMSE = \sqrt{\frac{\sum_j^n \left(y_{i,\,\exp} - y_{i,\,pred}\right)^2}{n}} \tag{11}$$

$$MAE = \frac{\sum_j^n \left|y_{i,\,\exp} - y_{i,\,pred}\right|}{n} \tag{12}$$

k-Fold Cross-Validation

To mitigate overfitting and enhance generalization performance and model stability, the k-fold cross-validation technique was employed. This method involves randomly partitioning the available dataset into k subsets (or folds). In each iteration, a model is trained on k−1 folds and validated on the remaining fold. A common and widely adopted value for k is 5, which was used in this study to evaluate all machine learning models employed here, including ANNs, RF, and SVM. By iterating this process across all k folds, out-of-fold predictions were generated, enabling a robust assessment of model performance on the entire dataset (Maleki et al. 2020; Teodorescu and Obreja Brașoveanu 2025).

Results

All ML models were trained using the MATLAB R2017a software package on a Windows 11 system equipped with an Intel® Celeron® N5105 processor (4 cores, 2.0 GHz) and 16 GB of RAM.

Artificial Neural Networks-Based modeling

Experimental data for developing the ANNs models for the three thermodynamic properties (ΔH, ΔS, and ΔG) are available in Table S1 of the supporting material file. Prior to developing the ANNs architectures for the thermodynamic properties (ΔH, ΔS, and ΔG), both the inputs and outputs were standardized according to Eq. (6). This preprocessing step is crucial for ensuring stable and rapid convergence during training, enhancing optimizer efficiency, and preventing numerical instabilities that hinder the network's ability to learn.

Table 1 presents the optimal ANNs architectures for modeling the three thermodynamic properties. All selected networks consist of a single hidden layer. These architectures were chosen based on their superior performance, demonstrated by lower MSE, RMSE, and MAE values, coupled with a higher R^2 value. On the training, validation, and testing data, the model demonstrates low prediction errors, with MAE, MSE, and RMSE values that are small relative to the scale of the target variable. Furthermore, the R^2 value is high. However, to confirm excellent model fitting and generalizability, these results must be validated on a held-out test set.

Table 1. Goodness-of-fit statistics (R^2, MAE, RMSE) for the developed ANNs models.

			Metrics to evaluate the fitted ANNs			
Thermodynamic property	**ANNs In-neuron-Out Hidden layer**	**Proof**	**MAE**	**MSE**	**RMSE**	**R^2**
ΔH	(2-10-1)	Training	0.0186	0.0006	0.0236	0.9999
		Validation	0.0931	0.0212	0.1456	0.9999
		Testing	0.0485	0.0061	0.0780	0.9999
		Overall	**0.0342**	**0.0045**	**0.0670**	**0.9999**
ΔS	(2-8-1)	Training	0.0001	0.0000	0.0001	0.9999
		Validation	0.0004	0.0000	0.0007	0.9999
		Testing	0.0002	0.0000	0.0003	0.9999
		Overall	**0.0001**	**0.0000**	**0.0003**	**0.9999**
ΔG	(2-10-1)	Training	0.0046	0.0000	0.0057	0.9999
		Validation	0.0821	0.0298	0.1727	0.9974
		Testing	0.0240	0.0027	0.0517	0.9995
		Overall	**0.0192**	**0.0049**	**0.0704**	**0.9993**

Based on the k-fold cross-validation analysis of an artificial neural network (ANNs) predicting thermodynamic properties (ΔH, ΔS, and ΔG), the model's performance and robustness were systematically evaluated across multiple data subsets. Figure S1 shows the distribution of R^2, MAE, and RMSE across folds, which were designed to assess the model's consistency and generalizability. A reliable model would demonstrate high, stable R^2 values and low, consistent error metrics (MAE and RMSE) for all three properties, with tight distributions in the box plots indicating that performance is not highly dependent on a specific data split. This comprehensive evaluation confirms whether the ANNs provides accurate and transferable predictions for thermodynamic parameters, which is crucial for its practical application.

Table 2. K-fold cross-validation results for ANNs predicting thermodynamic properties (ΔH, ΔS, and ΔG).

			Metrics to evaluate the fitted ANNs			
Thermodynamic property	**ANNs In-neuron-Out Hidden layer**	**Fold**	**MAE**	**MSE**	**RMSE**	**R^2**
ΔH	(2-10-1)	1	0.0114	0.0002	0.0155	0.9999
		2	0.8965	1.5605	1.2492	0.9941
		3	0.2117	0.1464	0.3827	0.9995
		4	0.1198	0.0240	0.1549	0.9999
		5	0.0725	0.0119	0.1092	0.9999
			Average R^2 score 0.9987±0.0026			
ΔS	(2-8-1)	1	0.0027	0.0000	0.0042	0.9906
		2	0.0017	0.0000	0.0025	0.9972
		3	0.0015	0.0000	0.0031	0.9960
		4	0.0002	0.0000	0.0002	0.9999
		5	0.0010	0.0000	0.0015	0.9992
			Average R^2 score 0.9966±0.0037			
ΔG	(2-10-1)	1	0.0414	0.0143	0.1197	0.9978
		2	0.0032	0.0000	0.0057	0.9999
		3	0.3705	1.0387	1.0191	0.8712
		4	0.0579	0.0070	0.0839	0.9981
		5	0.0249	0.0046	0.0682	0.9995
			Average R^2 score 0.9733±0.0571			

The predictive accuracy of the ANNs models was validated using parity plots comparing predicted and reference values for the primary thermodynamic properties (ΔH, ΔS, and ΔG). As shown in Figure 4, the ANNs models achieved an excellent correlation with the reference data, quantified by exceptionally high coefficients of determination (R^2). The R^2 values were 0.999969 for ΔH, 0.999928 for ΔS, and 0.999953 for ΔG. The precise prediction of ΔG is particularly important, as it is the key determinant spontaneity. The simultaneous, high-fidelity prediction of all three parameters confirms the model's internal consistency and its correct representation of the fundamental thermodynamic relationship, $\Delta G = \Delta H - T\Delta S$. The collective evidence from these parity plots demonstrates that the model is robust. The consistency of the R^2 values, all exceeding 0.9999, indicates a level of accuracy suitable for multiple applications. These ANNs models can thus be confidently employed to accurately forecast thermodynamic behavior, potentially reducing the need for extensive experimental characterization in future research.

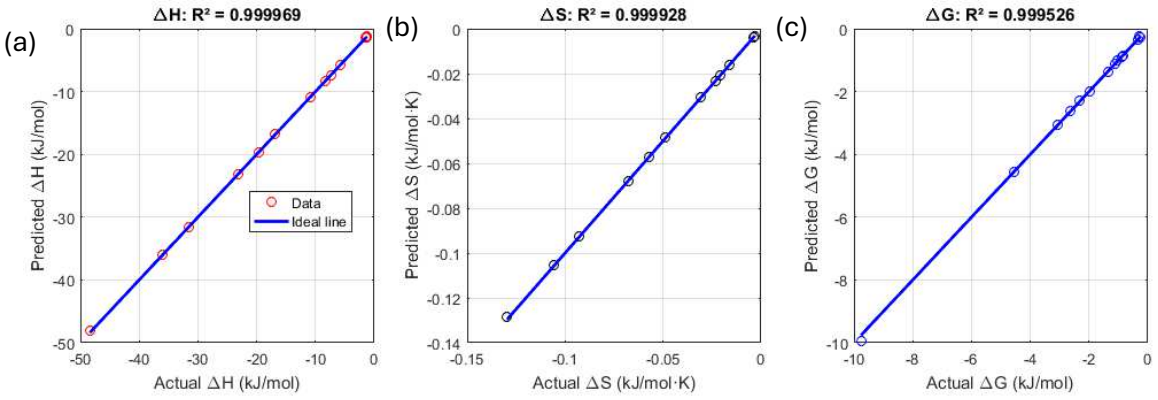

Fig. 4. Parity plots comparing predicted versus reference values for thermodynamic properties (a) ΔH, (b) ΔS, and (c) ΔG across all ANNs architectures. The dashed line indicates the ideal $y = x$ relationship.

The predictive performance of the ANNs is visualized in Figure 5, which depicts the modeled surfaces for ΔH, ΔS, and ΔG as functions of temperature and moisture content. The contours clearly reveal the non-linear nature of these relationships. Furthermore, the strong concordance between the model surfaces and the experimental data points confirms the excellent predictive capability of the ANNs.

The energy landscape of sorption is quantified in the 3D surface and contour plots (Figure 5a, d). The steep negative gradient at low moisture content ($\partial(\Delta H)/\partial M >> 0$) corresponds to a high isosteric heat of sorption, reaching values on the order of -60 kJ/mol for the strongest binding sites; this is a critical parameter for dryer design. As moisture content increases, the gradient flattens to a near-plateau approaching the enthalpy of vaporization of water (-44 kJ/mol). This signifies a transition from the regime of chemisorption and monolayer coverage to that of physisorption and capillary condensation.

The entropy profiles (Figures 5b and 5c) exhibit a steep negative gradient in ΔS at low moisture content (M). This trend quantifies the dramatic loss of configurational freedom, with ΔS values plunging below –0.15 kJ/mol K. The subsequent plateau, where ΔS approaches zero at higher M, signifies that the adsorbed water layer has attained sufficient mobility for its entropy to converge with that of bulk liquid water. This boundary behavior is critical for understanding the mobility and state of water within the material.

The interpretation of the ΔG plots (Figures 5e and 5f) is anchored by the spontaneity threshold ($\Delta G = 0$). Technically, this requires identifying the specific contour in Figure 5f where $\Delta G = 0$, which defines the exact conditions where sorption becomes non-spontaneous. For example, at a moisture content of 10 kg/100 kg, spontaneity is lost above 302 K—a vital operational limit. The thermodynamic driver for this behavior is revealed through a cross-property analysis: at low moisture content, the strongly negative ΔH dominates, overcoming the penalty from the similarly negative ΔS. As visually confirmed by the 3D surface in Figure 5e, rising temperature amplifies the -TΔS term, elevating the entire ΔG landscape and increasingly favoring desorption. The positive gradient, $\partial(\Delta G)/\partial T > 0$, is a direct graphical representation of a fundamental thermodynamic identity, thereby confirming the model's physical consistency.

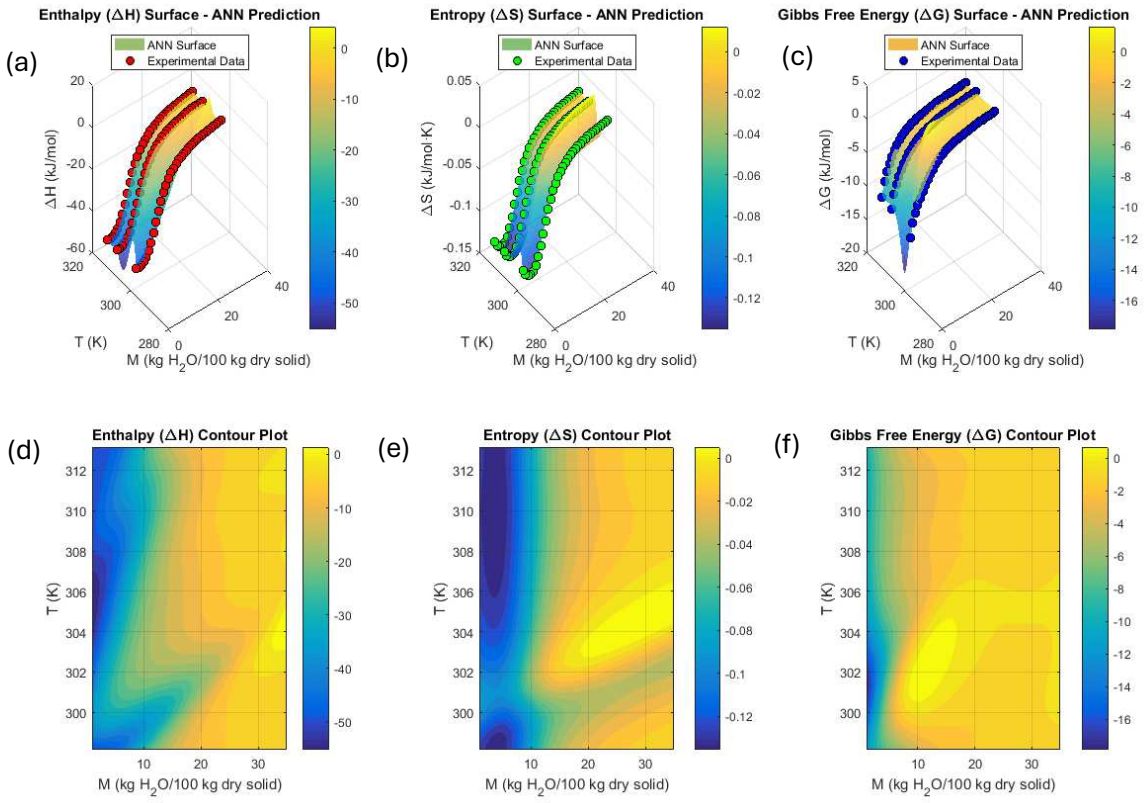

Fig. 5. ANNs model-predicted variation of thermodynamic properties. Surface and contour plots for (a, d) enthalpy change (ΔH), (b, e) entropy change (ΔS), and (c, f) Gibbs free energy change (ΔG) as functions of Moisture and Temperature. The contour plots (d-f) provide a two-dimensional projection of the surfaces shown in (a-c).

In the next two subsections (3.2 and 3.3), the predictive performance of Random Forest (RF) and Support Vector Machine (SVM) models was evaluated against an ANNs for predicting ΔH, ΔS, and ΔG based on temperature and moisture content, to identify the most robust model and avoid potential overfitting.

Randon Forest-Based Modeling

Experimental data for developing the RF models for the thermodynamic properties (ΔH, ΔS, and ΔG) are provided in Table S1. Prior to model development, the input and output variables were standardized using Eq. (7). This preprocessing step is essential for stabilizing the training process, accelerating convergence, and improving the overall performance of the models.

Table 3 presents the optimal Random Forest configuration for modeling the three thermodynamic properties, defined by its tuned hyperparameters: utilizing 50, 100, and 20 trees for ΔH, ΔS, and ΔG, respectively. This configuration was selected for its superior performance, as evidenced by lower MSE, RMSE, and MAE values and a higher R^2 score on the validation data. The model's strong generalizability is confirmed by its consistently low error metrics and high R^2 on a held-out test set.

Table 3. Goodness-of-fit statistics (R^2, MAE, RMSE) for the developed RF models.

			Metrics to evaluate the fitted RF			
Thermodynamic property	**Number of Trees**	**Proof**	**MAE**	**MSE**	**RMSE**	**R^2**
ΔH	50	Training	3.8384	24.5245	4.9522	0.9074
		Validation	5.9063	54.7509	7.3994	0.8624
		Testing	3.8274	24.4358	4.9433	0.8754
		Overall	**4.1519**	**29.1178**	**5.3961**	**0.8979**
ΔS	100	Training	0.0112	0.0002	0.0138	0.9096
		Validation	0.0164	0.0004	0.0205	0.8608
		Testing	0.0096	0.0001	0.0119	0.9091
		Overall	**0.0118**	**0.0002**	**0.0148**	**0.9024**
ΔG	20	Training	0.4677	0.7456	0.8635	0.8685
		Validation	1.0722	3.0510	1.7467	0.7304
		Testing	0.5805	1.0013	1.0007	0.8225
		Overall	**0.5759**	**1.1335**	**1.0646**	**0.8326**

The performance and robustness of the random forest (RF) model for predicting thermodynamic properties (ΔH, ΔS, and ΔG) were evaluated using k-fold cross-validation. The distributions of R^2, MAE, and RMSE scores across the folds are shown in Figure S2, providing a measure of model consistency and generalizability. For a reliable model, these distributions should be tight, indicating high, stable R^2 values and low, consistent error metrics across all three properties, with minimal dependence on a specific data split. This analysis confirms the extent to which the RF model provides accurate and transferable predictions for the target thermodynamic parameters.

Table 4. K-fold cross-validation results for RF predicting thermodynamic properties (ΔH, ΔS, and ΔG).

			Metrics to evaluate the fitted RF			
Thermodynamic property	**Number of Trees**	**Fold**	**MAE**	**MSE**	**RMSE**	**R^2**
ΔH	50	1	4.1189	22.9044	4.7859	0.9011
		2	3.0246	14.0391	3.7469	0.9473
		3	3.8291	24.7301	4.9729	0.9224
		4	3.0826	13.8588	3.7227	0.936
		5	3.7725	20.2575	4.5008	0.9461
		Average R^2 score 0.9306±0.0193				
ΔS	100	1	0.0112	0.0002	0.0127	0.9137
		2	0.0100	0.0001	0.0117	0.9375
		3	0.0111	0.0002	0.0139	0.9216
		4	0.0063	0.0001	0.0081	0.9621
		5	0.0109	0.0002	0.0137	0.9344
		Average R^2 score 0.9339±0.0185				
ΔG	20	1	0.6447	1.4311	1.1963	0.7796
		2	0.6365	0.663	0.8143	0.8648
		3	0.7196	1.3947	1.181	0.8271
		4	0.3329	0.203	0.4506	0.9445
		5	0.7551	1.9277	1.3884	0.8096
		Average R^2 score 0.84513±0.0635				

The performance of the RF models was validated by comparing predicted thermodynamic properties (ΔH, ΔS, and ΔG) to their reference values, as visualized in the parity plots of Figure 6. The models demonstrate excellent predictive power, reflected in high coefficients of determination: $R^2 = 0.9454$ for ΔH, 0.9414 for ΔS, and 0.9220 for ΔG. Notably, the accurate prediction of ΔG is crucial, as it is the key metric for assessing process spontaneity. The consistently high R^2 values across all three properties underscore the model's robustness and reliability. This validation confirms that RF models are a powerful tool for forecasting thermodynamic behavior, with the potential to streamline research by supplementing or reducing the need for extensive experimental characterization.

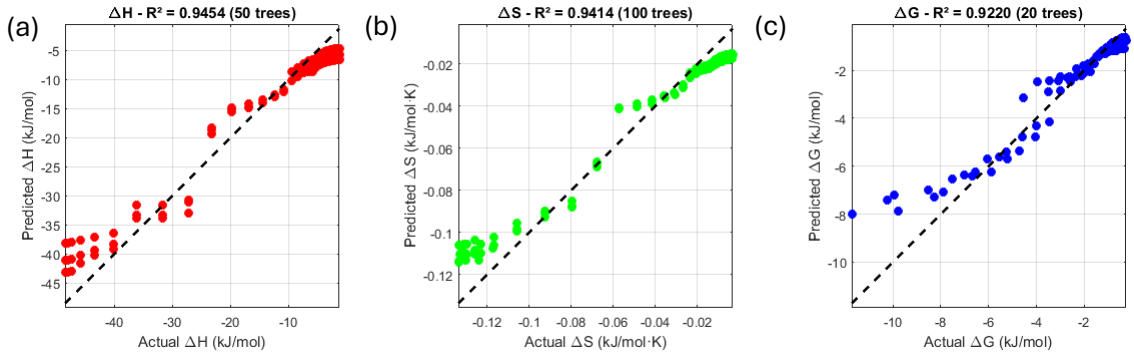

Fig. 6. Parity plots of predicted vs. reference values for (a) ΔH, (b) ΔS, and (c) ΔG from all RF models. The dashed line indicates the ideal $y = x$ relationship.

Figure 7 presents the RF model predictions for the key thermodynamic properties (ΔH, ΔS, and ΔG) as functions of temperature and moisture content. The 3D surface plots (Figures a-c), and corresponding 2D contour maps (Figures d-f) visualize the response of each property. Distinct RF models were trained for each property, utilizing 50, 100, and 20 trees for ΔH, ΔS, and ΔG, respectively. A consistent color scale is used across all plots, where negative values are represented by cool colors (blue) and values approaching zero by warm colors (yellow/red), facilitating direct comparison.

The predicted thermodynamic behavior is consistent with established physical principles for water sorption in biological materials. The enthalpy change (ΔH, Figures 7a, d) is strongly negative at low moisture levels and temperatures, indicating high-energy binding to primary sites. This exothermicity diminishes as moisture content increases, consistent with the occupancy of these high-affinity sites and subsequent sorption at less energetically favorable locations. The entropy change (ΔS, Figures 7b, e) is negative across the entire domain, reflecting a loss in molecular freedom of the water molecules upon sorption. The magnitude of this negative ΔS decreases with increasing moisture and temperature, suggesting a reduction in the ordering effect as the sorption matrix becomes hydrated and thermal motion increases.

The Gibbs free energy (ΔG, Figures 7c, f) is negative throughout the parameter space, confirming the spontaneity of the sorption process. The magnitude of ΔG decreases with increasing moisture content, signaling a reduction in driving force as the system approaches saturation. The influence of temperature on ΔG within the studied range is comparatively minor.

In summary, the RF models successfully capture complex, non-linear relationships in the sorption system, producing smooth and physically plausible surfaces. The analysis demonstrates that moisture content is the dominant factor governing the sorption thermodynamics, while temperature exerts a secondary influence. These insights are critical for food engineering applications, such as optimizing storage conditions and predicting product stability, as they quantify how environmental variables directly impact water binding energetics.

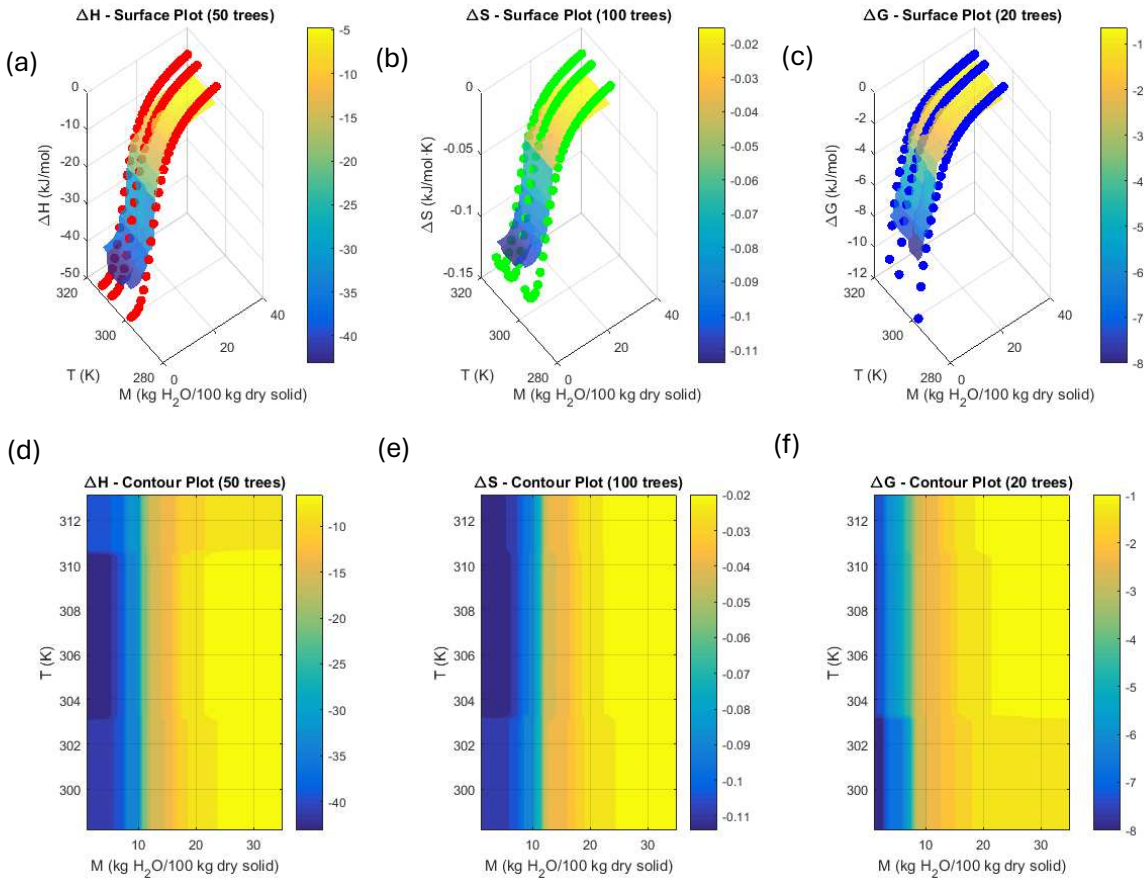

Fig. 7. SF model-predicted variation of thermodynamic properties. Surface and contour plots for (a, d) enthalpy change (ΔH), (b, e) entropy change (ΔS), and (c, f) Gibbs free energy change (ΔG) as functions of Moisture and Temperature. The contour plots (d-f) provide a two-dimensional projection of the surfaces shown in (a-c).

Support Vector Machine-Based Modeling

The experimental data used to develop the SVM models for predicting thermodynamic properties (ΔH, ΔS, and ΔG) are listed in Table S1. Before model development, all input and output variables were standardized via Eq. (8) to stabilize the training process, accelerate convergence, and enhance model performance.

Table 5 shows the best-performing SVM models, which all use the RBF kernel to predict three thermodynamic properties. Their high accuracy and strong generalizability are confirmed by low error rates and a high R^2 value across all data phases.

Table 5. Goodness-of-fit statistics (R^2, MAE, RMSE) for the developed SVM models.

		Metrics to evaluate the fitted SVM			
Thermodynamic property	**Proof**	**MAE**	**MSE**	**RMSE**	**R^2**
ΔH	Training	1.3657	2.0348	1.4265	0.9928
	Validation	1.5115	2.5030	1.5821	0.9914
	Testing	1.3986	2.2049	1.4849	0.9919
	Overall	**1.3926**	**2.1305**	**1.4596**	**0.9925**
ΔS	Training	0.0039	0.0000	0.0042	0.9920

	Validation	0.0048	0.0000	0.0055	0.9874
	Testing	0.0041	0.0000	0.0045	0.9907
	Overall	**0.0040**	**0.0000**	**0.0045**	**0.9911**
ΔG	Training	0.3756	0.9898	0.9949	0.8655
	Validation	0.2606	0.1827	0.4274	0.9631
	Testing	0.3038	0.4127	0.6424	0.9275
	Overall	**0.3478**	**0.7844**	**0.8856**	**0.8841**

The performance and robustness of the support vector machine (SVM) model for predicting thermodynamic properties (ΔH, ΔS, and ΔG) were rigorously assessed via k-fold cross-validation. Figure S3 presents the distributions of R^2, MAE, and RMSE across the folds. The model demonstrates high, stable R^2 values and low, consistent error metrics for all three properties. The tight distributions observed in the box plots indicate that the model's performance is robust and not dependent on a specific data split. This comprehensive evaluation confirms that the SVM provides accurate and generalizable predictions for thermodynamic parameters, underscoring its utility for practical application.

Table 6. K-fold cross-validation results for SVM predicting thermodynamic properties (ΔH, ΔS, and ΔG).

		Metrics to evaluate the fitted SVM			
Thermodynamic property	**Fold**	**MAE**	**MSE**	**RMSE**	**R^2**
ΔH	1	1.7454	3.2765	1.8101	0.9859
	2	1.7088	3.1827	1.7840	0.9880
	3	1.5370	2.6543	1.6292	0.9917
	4	1.6892	3.0941	1.7590	0.9857
	5	1.4086	2.2822	1.5107	0.9939
	Average R^2 score 0.9890±0.0036				
ΔS	1	0.0047	0.0000	0.0050	0.9862
	2	0.0052	0.0000	0.0055	0.9862
	3	0.0039	0.0000	0.0044	0.9922
	4	0.0043	0.0000	0.0046	0.9877
	5	0.0036	0.0000	0.0042	0.994
	Average R^2 score 0.9893±0.0036				
ΔG	1	0.3515	0.9164	0.9573	0.8589
	2	0.1843	0.0927	0.3045	0.9811
	3	0.4517	1.0146	1.0073	0.8742
	4	0.2112	0.1224	0.3499	0.9665
	5	0.4558	1.0155	1.0077	0.8997
	Average R^2 score 0.9161±0.0549				

The performance of the SVM models was validated by comparing the predicted thermodynamic properties (ΔH, ΔS, and ΔG) with their reference values, as visualized in the parity plots of Figure 8. The models for ΔH and ΔS demonstrated excellent predictive power, indicated by high coefficients of determination (R^2 = 0.9914 and 0.9906, respectively). In comparison, the model for ΔG exhibited slightly lower, yet still strong, predictive power (R^2 = 0.8843). This relative difficulty is exemplified in Figure 8c, which demonstrates the specific challenge of modeling ΔG as its value becomes more negative. In contrast, the consistently high R^2 values for ΔH and ΔS underscore the model's underlying robustness. This overall performance confirms that

the SVM approach is a powerful tool for forecasting thermodynamic behavior, with the potential to streamline research by supplementing or reducing the need for extensive experimental characterization.

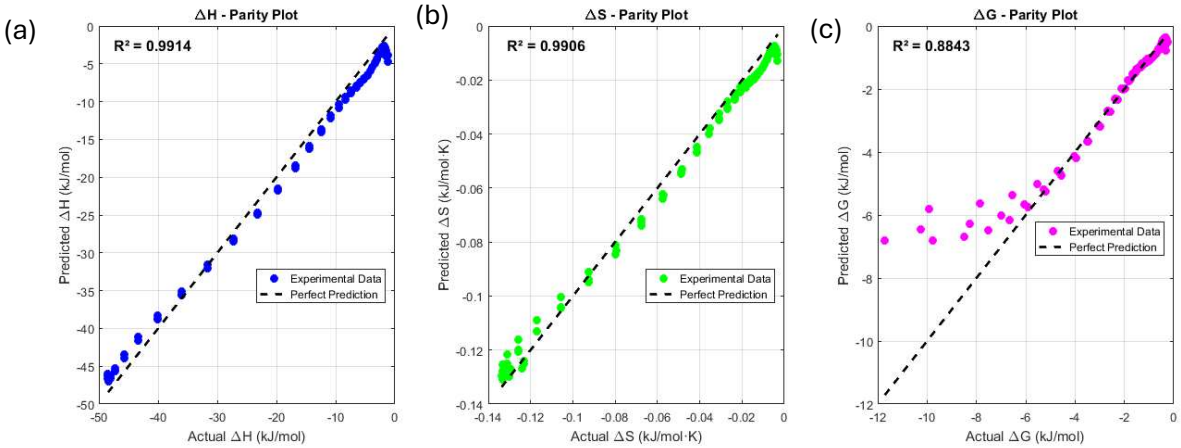

Fig. 8. Parity plots comparing Support Vector Machine (SVM) predicted versus reference values for thermodynamic properties: (a) ΔH, (b) ΔS, and (c) ΔG. The dashed line indicates the ideal $y = x$ relationship.

Figure 9 presents surface and contour plots illustrating the dependence of the thermodynamic parameters (ΔH, ΔS, and ΔG) on temperature (T) and moisture content (M). The close agreement between the SVM model predictions and the experimental data across all plots validates the model's accuracy in characterizing the system's thermodynamic behavior.

The plots reveal that both ΔH and ΔS increase with rising temperature and moisture content (Figures 9a, b, d, e). The positive values of ΔH confirm the endothermic nature of the process, requiring greater energy input at higher T and M. The concomitant increase in ΔS suggests a corresponding increase in molecular disorder and randomness.

In contrast, ΔG decreases with increasing temperature (Figures 9c, f), indicating that the process becomes more spontaneous at elevated temperatures. The negative ΔG values, particularly within the contours of the lower-right quadrant of the plot, delineate the operational zones where the reaction driving force is most pronounced. This underscores the dominant role of temperature in governing process feasibility.

Collectively, these trends describe an endothermic, entropy-driven process that gains spontaneity with increasing thermal energy. These findings provide critical insights into the energy requirements and equilibrium states of the system, confirming the SVM model's utility for optimizing thermal and drying processes.

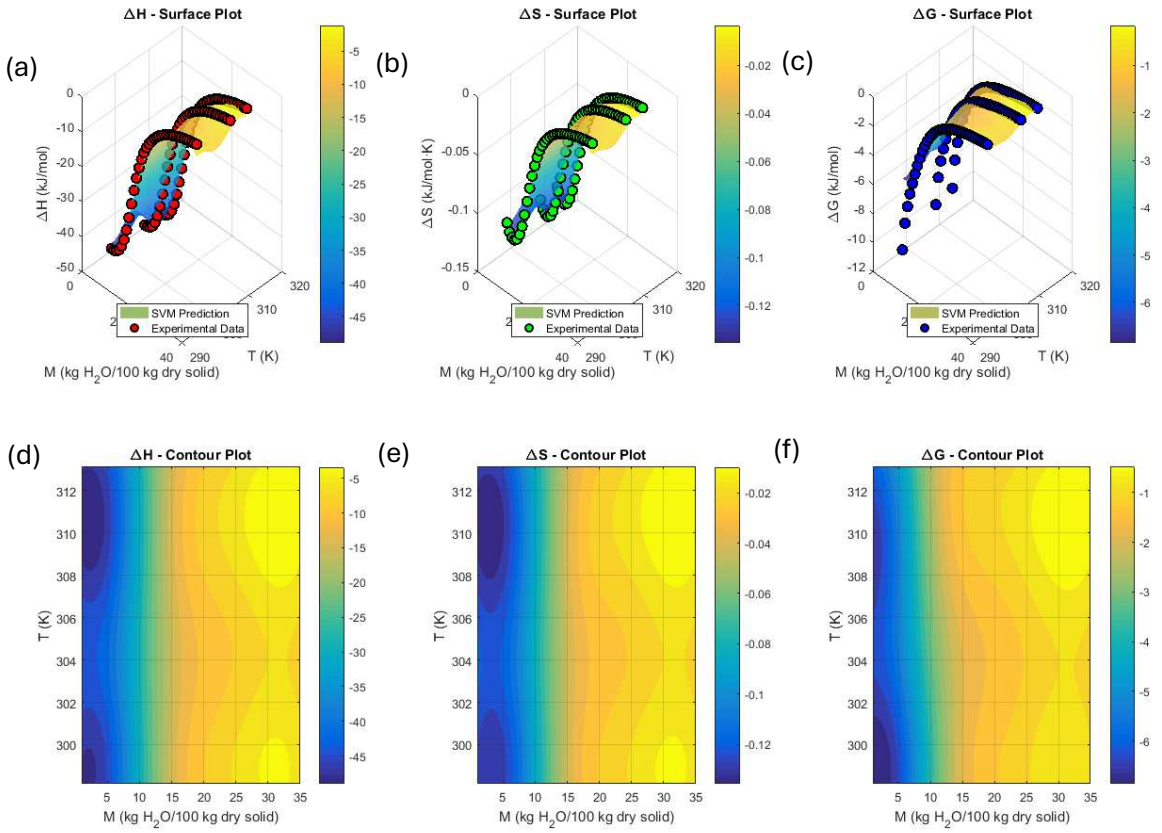

Fig. 9. SVM model-predicted variation of thermodynamic properties. Surface and contour plots for (a, d) enthalpy change (ΔH), (b, e) entropy change (ΔS), and (c, f) Gibbs free energy change (ΔG) as functions of Moisture and Temperature. The contour plots (d-f) provide a two-dimensional projection of the surfaces shown in (a-c).

Discussion

K-fold cross-validation (Tables 2, 4, and 6) reveals that the ANNs and SVM models both provide excellent predictions for ΔH and ΔS. For ΔG, however, only the ANNs model yields accurate predictions, as further supported by the 3D prediction surfaces (Figures 5, 7, and 9).

The performance of machine learning models (ANNs, RF, SVM) for predicting thermodynamic properties (ΔH, ΔS, ΔG) is summarized in Figure 10. Four bar charts compare the models using MAE, MSE, RMSE, and R^2 metrics: three charts for the individual properties and a fourth for the average performance across all properties.

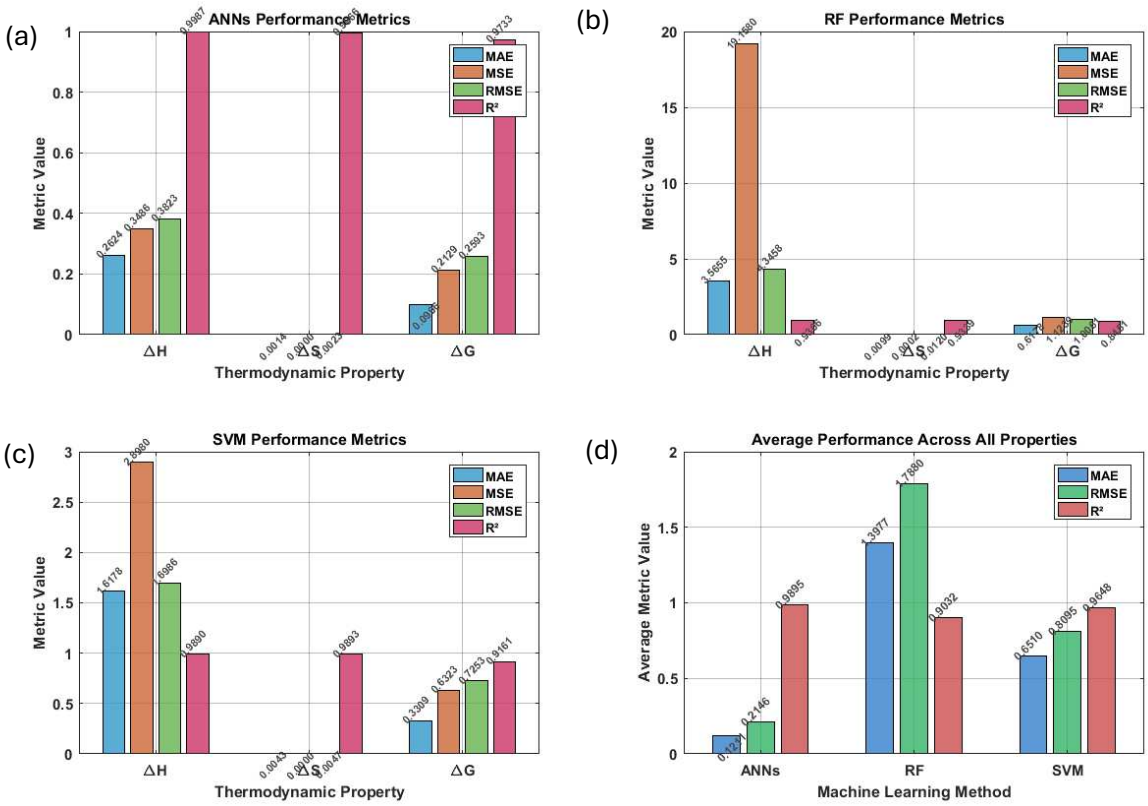

Fig. 10. Metric comparison of the machine learning method for the three thermodynamic properties (ΔH, ΔS, and ΔG).

Figure 10a presents the performance of the ANNs model across the three thermodynamic properties, demonstrating exceptional consistency and accuracy. The model achieves an R^2 of 0.9987 for ΔH, with an MAE of 0.2624 and RMSE of 0.3823. For ΔS, it attains an R^2 of 0.9966 and an MAE of 0.0014, indicating near-perfect precision. Performance for ΔG remains high, with an R^2 of 0.9733 and an RMSE of 0.2593. Visually, the high R^2 values and short error bars for all properties underscore the model's robustness. These results establish the ANNs as a highly capable model for capturing the complex physical relationships underlying these thermodynamic quantities.

In Figure 10b, the performance of the RF model presents a dramatic contrast to Figure 10a. While RF achieves a respectable R^2 of 0.9339 for ΔS (with a modest MAE of 0.0099), its performance deteriorates sharply for the other properties. For ΔH, the RMSE surges to 4.3458—the largest error for any model in the figure—reflecting a significant failure to model enthalpy accurately. Similarly, for ΔG, the R^2 drops to 0.8451, the lowest among all model-property combinations, and its RMSE (1.0061) is an order of magnitude higher than that of ANNs. This visual imbalance underscores RF's fundamental inconsistency. The model works well for entropy but struggles profoundly with enthalpy and free energy, likely due to its difficulty in capturing the continuous, nonlinear relationships that characterize these properties.

As shown in Figure 10c, the SVM model demonstrated intermediate yet consistent performance, outperforming RF but not matching the accuracy of the ANNs. For ΔH, SVM achieved an R^2 of 0.989 and an RMSE of 1.6986; for ΔS, R^2 = 0.9893 with a minimal RMSE; and for ΔG, R^2 = 0.9161 with an RMSE of 0.7253. The moderate and balanced bar heights in the figure reflect this reliability. These results position SVM as a robust and computationally efficient alternative for thermodynamic prediction, especially in scenarios where the highest precision is not critical.

Finally, Figure 10d synthesizes the results, presenting the mean performance of each model across all three thermodynamic properties. As the definitive summary of the study, this panel demonstrates a commanding lead for ANNs, which achieved the highest R^2 (≈0.9895) alongside the lowest MAE (≈0.1211) and RMSE (≈0.1473). This is visually confirmed by their tallest R^2 bar and shortest error bars. SVMs follow at a distinct but consistent margin, while RF trails significantly behind, evident in its notably shorter R^2 bar and substantially longer error bars. Collectively, these results solidify the conclusion that ANNs are not only superior for predicting individual properties but also represent the most robust and generalizable approach overall.

Together, Figures 10a–10d provide a compelling visual narrative that is fully supported by the numerical data. They reveal not only the top-performing algorithm but also how each one behaves differently across the thermodynamic landscape. The ease of predicting ΔS (evident in all panels) contrasts sharply with the difficulty of modeling ΔG and especially ΔH for traditional machine learning methods. Ultimately, Figure 10 demonstrates that Artificial Neural Networks (ANNs) are the unequivocally optimal choice for the accurate, reliable, and consistent prediction of ΔH, ΔS, and ΔG. Among the alternatives, Support Vector Machines present a viable secondary option, whereas Random Forest (RF) is ill-suited for this specific scientific regression task.

The analysis of computational cost is a critical factor in model selection, as it balances predictive performance against practical deployment constraints. In this study, a clear trade-off is observed between the accuracy of the models and their computational demands.

The ANNs achieved the highest accuracy in approximating the target thermodynamic properties, establishing themselves as the superior model in terms of predictive performance. However, this excellence comes at a high computational and energetic cost. The ANNs required a training time of 154.6 seconds, which is an order of magnitude greater than the ensemble and kernel-based methods tested. Specifically, it was approximately 17 times slower than RF at 9.1 s and 27 times slower than SVM at 5.8 s.

To quantify the environmental and operational impact, we can estimate energy consumption during training. Using a standard approximation for average power draw of a high-performance computing CPU/GPU under load (~150 Watts) (Azimi et al. 2020), the energy consumed (in Joules) is calculated as Energy = Power × Time, as is displayed in Table 7.

Table 7. Estimated energy consumption for each ML approach.

Model	Computing Time (s)	Estimated Energy Consumption (Joules)	Relative Energy Factor
ANNs	154.6	~23,190 J	1.0 (Baseline)
RF	9.1	~1,365 J	~0.06
SVM	5.8	~870 J	~0.04

This estimation reveals the profound energetic implications of the runtime disparity. For a single training run, the ANNs consume over 16 and 26 times more energy than the RF and SVM models, respectively. In large-scale hyperparameter tuning involving hundreds or thousands of iterations, this difference escalates from kilojoules to megajoules of additional energy consumption, leading to substantially higher operational costs and presumably to a larger carbon footprint.

The selection of an appropriate model is highly dependent on the specific application context:

- In high-fidelity, offline applications where maximum prediction accuracy is the primary objective and model deployment is infrequent (such as a final property calculator in a published design suite), artificial neural networks (ANNs) are the most appropriate choice despite their higher computational and energy demands.

- For rapid prototyping, iterative design, or applications requiring frequent retraining on new data (e.g., adaptive models in process control), the RF and SVM models present a far more efficient and sustainable alternative. Their low energy footprint enables faster and more cost-effective research cycles, making them preferable in resource-constrained environments.

Hence, while the ANNs provides the best approximation of the thermodynamic properties, its computational time and associated energy consumption are significantly higher. The RF and SVM models offer a compelling compromise, delivering results with excellent computational and energetic efficiency. Future work could focus on optimizing the ANNs architecture (e.g., via pruning, quantization) or leveraging specialized hardware to bridge this performance-efficiency gap, making high-accuracy models more sustainable.

The weights and biases for the ANNs models of the three thermodynamic properties are provided in the Appendix.

Conclusions

Based on the findings of this study, the following conclusions can be drawn:

- This study successfully developed and compared three machine learning models (ANNs, RF, and SVM) for predicting the thermodynamic properties (ΔH, ΔS, and ΔG) of sacred pepper (*Piper auritum*) leaf as functions of moisture content and temperature.
- The key findings conclusively demonstrate that Artificial Neural Networks (ANNs) are the superior model for this specific regression task. The ANNs model consistently achieved the highest predictive accuracy and robustness across all three thermodynamic properties, as evidenced by near-perfect coefficients of determination ($R^2 > 0.999$ for ΔH and ΔS, and 0.9993 for ΔG overall) and the lowest error metrics (MAE, RMSE) in both standard and k-fold cross-validation analyses. Its ability to accurately capture complex, nonlinear relationships and maintain physical consistency, particularly for the critical parameter ΔG, underscores its exceptional capability.
- In contrast, the Support Vector Machine (SVM) model provided reliable, intermediate performance, serving as a competent but less accurate alternative. The Random Forest (RF) model was the least effective, exhibiting significant performance degradation, especially for predicting ΔH and ΔG, which highlights its limitations in modeling the continuous, intricate thermodynamic relationships in this system.
- Therefore, ANNs establish themselves as a powerful and highly accurate computational tool for predicting the thermodynamic behavior of sacred pepper leaf. The implementation of such a model can significantly reduce the reliance on extensive and costly experimental characterization in future research, facilitating more efficient process design and optimization in food engineering and related fields.

Acknowledgement

Authors Cesar Pérez-Alonso, Reyna Natividad, Ever Peralta-Reyes, and Alejandro Regalado-Méndez are grateful to the Secretary of Science, Humanities, Technology, and Innovation (SECIHTI) for the financial support through the Investigators National System Program (SNII) of Mexico.

Funding: This research received no external funding.

Data Availability: The datasets used and/or analyzed during the current study are available in the supplementary material. Another set is available upon reasonable request to the corresponding author.

Competing Interests: The authors declare no competing interests.

Appendix

In this section, the optimized model parameters (weights and biases) for the ANNs predicting the three thermodynamic properties (ΔH (Eq. (A2)), ΔS (Eq. (A3)), and ΔG (Eq. (A4))) are presented. Also, the general ANNs model is represented by Eq. (A1).

ANNs model prediction for the three thermodynamic properties

$$Y_{\Delta H,\,\Delta S,\,and\ \Delta G} = \sum_i \left[w_2 \times \tan sig \sum_i \left[X_i w_1 \right] + b_1 \right] + b_2 \tag{A1}$$

Model parameters of the ANNs for predicting ΔH

$$w_1 = \begin{bmatrix} -2.087978 & 3.348476 \\ -2.112867 & 4.685799 \\ 2.930416 & -5.447981 \\ -2.564162 & 3.042819 \\ -2.253661 & 0.233944 \\ -2.037772 & 4.379941 \\ -1.420762 & 3.259177 \\ 2.981406 & -1.541226 \\ 2.467170 & -2.573405 \\ 3.598908 & -3.223037 \end{bmatrix},\quad b_1 = \begin{bmatrix} 4.754004 \\ 2.877882 \\ -3.716403 \\ 1.102497 \\ 0.104729 \\ -1.288200 \\ -1.488397 \\ 2.256824 \\ 3.418446 \\ 5.100645 \end{bmatrix},\quad b_2 = 0.028732$$

$$w_2 = \begin{bmatrix} -0.064638 & 1.926604 & 1.848189 & -0.053693 & -0.238352\ldots \\ 0.138915 & -0.144979 & 1.399600 & -2.133789 & 1.449108 \end{bmatrix} \tag{A2}$$

Model parameters of the ANNs for predicting ΔS

$$w_1 = \begin{bmatrix} 1.497759 & -5.306030 \\ 0.737856 & -2.902471 \\ -1.779833 & 2.762295 \\ 3.577166 & 0.000846 \\ 1.409765 & -0.127751 \\ -2.867358 & -0.031117 \\ 0.276762 & 5.126322 \\ -2.713769 & -1.937795 \end{bmatrix},\quad b_1 = \begin{bmatrix} -2.960868 \\ -1.622985 \\ -1.190221 \\ 1.982406 \\ 0.877529 \\ -2.700902 \\ -3.701150 \\ -5.867974 \end{bmatrix},\quad b_2 = 0.488322$$

$$w_2 = \begin{bmatrix} -1.384987 & 1.438809 & -0.035028 & 0.829316\ \ldots \\ 0.778710 & 0.870153 & 0.049965 & 0.207345 \end{bmatrix} \tag{A3}$$

Model parameters of the ANNs for predicting ΔG

$$w_1 = \begin{bmatrix} 1.865392 & -4.321445 \\ 4.800363 & 1.861234 \\ 0.751145 & -3.734523 \\ -2.692288 & 1.903603 \\ 2.542513 & -2.430644 \\ -2.712534 & 3.134002 \\ -2.727546 & -1.405985 \\ -2.888357 & 0.513919 \\ 0.385055 & -3.593784 \\ 3.364128 & -0.634670 \end{bmatrix}, \quad b_1 = \begin{bmatrix} -4.376047 \\ -1.656395 \\ -3.079765 \\ -0.333564 \\ 0.748259 \\ -1.155713 \\ -3.300845 \\ -2.022175 \\ 4.354501 \\ 4.278196 \end{bmatrix}, \quad b_2 = -1.799825 \qquad \text{A4}$$

$$w_2 = \begin{bmatrix} 0.164133 & 0.019460 & -0.180991 & 1.922101 & 4.343336 & \dots \\ 2.257116 & -1.419312 & -0.243853 & -0.514933 & 1.461338 & \end{bmatrix}$$

References

Alpizar-Reyes, E., Carrillo-Navas, H., Romero-Romero, R., Varela-Guerrero, V., Alvarez-Ramírez, J., & Pérez-Alonso, C. (2017). Thermodynamic sorption properties and glass transition temperature of tamarind seed mucilage (Tamarindus indica L.). *Food and Bioproducts Processing*, *101*, 166–176. https://doi.org/10.1016/J.FBP.2016.11.006

Arslan-Tontul, S. (2020). Moisture sorption isotherm and thermodynamic analysis of quinoa grains. *Heat and Mass Transfer 2020 57:3*, *57*(3), 543–550. https://doi.org/10.1007/S00231-020-02978-8

Azimi, R., Jing, C., & Reda, S. (2020). PowerCoord: Power capping coordination for multi-CPU/GPU servers using reinforcement learning. *Sustainable Computing: Informatics and Systems*, *28*, 100412. https://doi.org/10.1016/J.SUSCOM.2020.100412

Bayless, Rick., & Bayless, D. Groen. (2024). *Authentic Mexican : regional cooking from the heart of Mexico* (1st ed.). New York: Harper Collins.

Ben Khedher, M. B., & Yun, D. (2024). An Interpretable Machine Learning-Based Hurdle Model for Zero-Inflated Road Crash Frequency Data Analysis: Real-World Assessment and Validation. *Applied Sciences 2024, Vol. 14, Page 10790*, *14*(23), 10790. https://doi.org/10.3390/APP142310790

Bensebia, O., & Allia, K. (2016). Analysis of adsorption–desorption moisture isotherms of rosemary leaves. *Journal of Applied Research on Medicinal and Aromatic Plants*, *3*(3), 79–86. https://doi.org/10.1016/J.JARMAP.2016.01.005

Birgen, C., Magnanelli, E., Carlsson, P., Skreiberg, Ø., Mosby, J., & Becidan, M. (2021). Machine learning based modelling for lower heating value prediction of municipal solid waste. *Fuel*, *283*, 118906. https://doi.org/10.1016/J.FUEL.2020.118906

Chayjan, R. A., & Esna-Ashari, M. (2011). Effect of moisture content on thermodynamic characteristics of grape: mathematical and artificial neural network modelling. *https://cjfs.agriculturejournals.cz/doi/10.17221/328/2009-CJFS.html*, *29*(3), 250–259. https://doi.org/10.17221/328/2009-CJFS

Chong, C. H., Dibagar, N., Maulion, R., & Figiel, A. (2023). Drying Characteristics of Herbs, Spices, and Medicinal Plants. *Drying of Herbs, Spices, and Medicinal Plants*, 29–52. https://doi.org/10.1201/9781003269250-3/DRYING-CHARACTERISTICS-HERBS-SPICES-

MEDICINAL-PLANTS-CHIEN-HWA-CHONG-NESA-DIBAGAR-RHONALYN-MAULION-ADAM-FIGIEL

Collazos-Escobar, G. A., Gutiérrez-Guzmán, N., Váquiro, H. A., García-Pérez, J. V., & Cárcel, J. A. (2025). Analysis of Machine Learning Algorithms for the Computer Simulation of Moisture Sorption Isotherms of Coffee Beans. *Food and Bioprocess Technology 2025 18:6*, *18*(6), 5419–5430. https://doi.org/10.1007/S11947-025-03785-X

Conde-Hernández, L. A., Espinosa-Victoria, J. R., & Guerrero-Beltrán, J. (2017). Supercritical extraction of essential oils of Piper auritum and Porophyllum ruderale. *The Journal of Supercritical Fluids*, *127*, 97–102. https://doi.org/10.1016/J.SUPFLU.2017.03.026

Conde-Hernández, L. A., & Guerrero-Beltrán, J. Á. (2014). Total phenolics and antioxidant activity of Piper auritum and Porophyllum ruderale. *Food Chemistry*, *142*, 455–460. https://doi.org/10.1016/J.FOODCHEM.2013.07.078

Davidow, Joie. (1999). *Infusions of healing : a treasury of Mexican-American herbal remedies* (1st ed.). New York: Simon & Schuster.

Davis, C. C., & Choisy, P. (2024). Medicinal plants meet modern biodiversity science. *Current Biology*, *34*(4), R158–R173. https://doi.org/10.1016/J.CUB.2023.12.038

de Holanda Rosanova, A., Maia, G. D., Freire, F. B., & do Carmo Ferreira, M. (2017). A Neural Based Modeling Approach for Drying Kinetics Analysis of Mint Branches and Their Fractions (Leaves and Stems). *Advances in Chemical Engineering and Science*, *07*(02), 154–174. https://doi.org/10.4236/ACES.2017.72012

Ekor, M. (2014). The growing use of herbal medicines: Issues relating to adverse reactions and challenges in monitoring safety. *Frontiers in Neurology*, *4 JAN*, 66193. https://doi.org/10.3389/FPHAR.2013.00177/BIBTEX

Geck, M. S., Cristians, S., Berger-González, M., Casu, L., Heinrich, M., & Leonti, M. (2020). Traditional Herbal Medicine in Mesoamerica: Toward Its Evidence Base for Improving Universal Health Coverage. *Frontiers in Pharmacology*, *11*, 541133. https://doi.org/10.3389/FPHAR.2020.01160/FULL

Kaur, K., Kumar, S., Kaur, P., Singh, R. P., & Grewal, I. S. (2024). Evaluation of mathematical models and artificial neural networks for prediction of sorption isotherm in microwave pre-heated mung bean. *Discover Food 2024 4:1*, *4*(1), 155-. https://doi.org/10.1007/S44187-024-00231-3

Liu, F., El-Mesery, H. S., ElMesiry, A. H., Hu, Z., & Salem, A. (2025). Predicting mass transfer activation energy and physicochemical properties of dried onion using numerical modeling and artificial intelligence. *Scientific Reports 2025 15:1*, *15*(1), 19463-. https://doi.org/10.1038/s41598-025-04814-7

Loganathan, V., Vijayan, L., & Rengaraju, B. (2025). Optimisation of Microwave-Assisted Extraction of Phenolic Compounds from Pithecellobium dulce Fruit Peels: Comparative Process Modelling Using RSM and ANN with Bioactivity Evaluation. *Processes 2025, Vol. 13, Page 3554*, *13*(11), 3554. https://doi.org/10.3390/PR13113554

Maleki, F., Muthukrishnan, N., Ovens, K., Reinhold, C., & Forghani, R. (2020). Machine Learning Algorithm Validation: From Essentials to Advanced Applications and Implications for Regulatory Certification and Deployment. *Neuroimaging Clinics of North America*, *30*(4), 433–445. https://doi.org/10.1016/J.NIC.2020.08.004

Mason, R. L., Gunst, R. F., & Hess, J. L. (2023). *Statistical Design and Analysis of Experiments With Applications to Engineering and Science Second Edition* (2nd ed.). NJ: John Wiley & Sons: Hoboken. Accessed 24 October 2025

McBurnett, B. G., Chavira, A. A., López, A. C., Mosso, J., & Collins, S. M. (2007). Analysis of Piper auritum: A traditional hispanic herb. *ACS Symposium Series*, *946*, 67–76. https://doi.org/10.1021/BK-2007-0946.CH006

Okamura, M., Soga, M., Yamada, Y., Kobata, K., & Kaneda, D. (2021). Development and evaluation of roasting degree prediction model of coffee beans by machine learning. *Procedia Computer Science*, *192*, 4602–4608. https://doi.org/10.1016/J.PROCS.2021.09.238

Pérez-Alonso, C., Beristain, C. I., Lobato-Calleros, C., Rodríguez-Huezo, M. E., & Vernon-Carter, E. J. (2006). Thermodynamic analysis of the sorption isotherms of pure and blended carbohydrate polymers. *Journal of Food Engineering*, *77*(4), 753–760. https://doi.org/10.1016/J.JFOODENG.2005.08.002

Rajawat, A. S., Mohammed, O., Shaw, R. N., & Ghosh, A. (2022). Renewable energy system for industrial internet of things model using fusion-AI. *Applications of AI and IOT in Renewable Energy*, 107–128. https://doi.org/10.1016/B978-0-323-91699-8.00006-1

Rashvand, M., Dehkharghanian, N., Nikzadfar, M., Javed, T., Luke, L. P., O'Brien, A., et al. (2025). Machine Learning-Driven Optimization for Digital Transformation in Non-thermal Food Processing. *Food and Bioprocess Technology 2025 18:12*, *18*(12), 10283–10316. https://doi.org/10.1007/S11947-025-04078-Z

Razzaghi, M., Karimi, A., Ansari, Z., & Aghdasinia, H. (2018). Phenol removal by HRP/GOx/ZSM-5 from aqueous solution: Artificial neural network simulation and genetic algorithms optimization. *Journal of the Taiwan Institute of Chemical Engineers*, *89*, 1–14. https://doi.org/10.1016/J.JTICE.2018.03.040

Rizvi, S. S. H. (2014). Thermodynamic Properties of Foods in Dehydration. *Engineering Properties of Foods: Third Edition*, 239–326. https://doi.org/10.1201/9781420028805-11/THERMODYNAMIC-PROPERTIES-FOODS-DEHYDRATION-RIZVI

Sánchez, Y., Pino, O., Correa, T. M., Naranjo, E., & Iglesia, A. (1986). Revista de protección vegetal. *Revista de protección vegetal*, *24*(1), 39–46. http://scielo.sld.cu/scielo.php?script=sci_arttext&pid=S1010-27522009000100006&lng=es&nrm=iso&tlng=es. Accessed 20 November 2025

Teodorescu, V., & Obreja Brașoveanu, L. (2025). Assessing the Validity of k-Fold Cross-Validation for Model Selection: Evidence from Bankruptcy Prediction Using Random Forest and XGBoost. *Computation 2025, Vol. 13, Page 127*, *13*(5), 127. https://doi.org/10.3390/COMPUTATION13050127

Ullah, H., Khan, S., Chen, B., Shahab, A., Riaz, L., Lun, L., & Wu, N. (2023). Machine learning approach to predict adsorption capacity of Fe-modified biochar for selenium. *Carbon Research 2023 2:1*, *2*(1), 29-. https://doi.org/10.1007/S44246-023-00061-5

Vapnik, V. N. (2000). Methods of Pattern Recognition. *The Nature of Statistical Learning Theory*, 123–180. https://doi.org/10.1007/978-1-4757-3264-1_6

Velásquez, S., Franco, A. P., Peña, N., Bohórquez, J. C., & Gutierrez, N. (2021). Effect of coffee cherry maturity on the performance of the drying process of the bean: Sorption isotherms and dielectric spectroscopy. *Food Control*, *123*, 107692. https://doi.org/10.1016/J.FOODCONT.2020.107692

Wang, P., Yang, X., Huang, X., Ma, G., Zhang, S., Wang, S., et al. (2025). Modeling and Optimization of Microwave Vacuum Drying for Pinelliae Rhizoma: Integrating Drying Kinetics, Artificial Neural Networks, and Quality Preservation. *Food Science and Nutrition*, *13*(8), e70672. https://doi.org/10.1002/FSN3.70672;WGROUP:STRING:PUBLICATION

Williams, N. H., Gupta, M. P., Arias, T. D., Bos, R., & Tattje, D. H. E. (2004). Safrole, the Main Component of the Essential Oil from Piper auritum of Panama. *Journal of Natural Products*, *48*(2), 330. https://doi.org/10.1021/NP50038A026

Yu, S., Zheng, H., Wilson, D. I., Yu, W., & Young, B. R. (2024). Integrating Image Analysis and Machine Learning for Moisture Prediction and Appearance Quality Evaluation: A Case Study of Kiwifruit Drying Pretreatment. *Foods 2024, Vol. 13, Page 1789*, *13*(12), 1789. https://doi.org/10.3390/FOODS13121789

Supplementary Files

This is a list of supplementary files associated with this preprint. Click to download.

- Graphicalabstract.tiff
- TableS1.docx
- TableS2.docx
- Supportingmaterialsv2.docx